Available online at www.sciencedirect.com
ScienceDirect
Trans. Nonferrous Met. Soc. China 32(2022) 1070−1082
Transactions of Nonferrous Metals Society of China
www.tnmsc.cn

Aging precipitation behavior and properties of Al−Zn−Mg−Cu−Zr−Er alloy at different quenching rates

Yi-chang WANG[1], Xiao-dong WU[1], Lu YUE[1], Ming-xing GUO[2], Ling-fei CAO[1,3]

1. International Joint Laboratory for Light Alloys (Ministry of Education), College of Materials Science and Engineering, Chongqing University, Chongqing 400044, China;
2. State Key Laboratory for Advanced Metals and Materials, University of Science and Technology Beijing, Beijing 100083, China;
3. Shenyang National Laboratory for Materials Science, Chongqing University, Chongqing 400044, China

Received 16 April 2021; accepted 14 September 2021

Abstract: The effect of quenching rate on the aging precipitation behavior and properties of Al−Zn−Mg−Cu−Zr−Er alloy was investigated. The scanning electron microscopy, transmission electron microscopy, and atom probe tomography were used to study the characteristics of clusters and precipitates in the alloy. The quench-induced η phase and a large number of clusters are formed in the air-cooled alloy with the slowest cooling rate, which contributes to an increment of hardness by 24% (HV 26) compared with that of the water-quenched one. However, the aging hardening response speed and peak-aged hardness of the alloy increase with the increase of quenching rate. Meanwhile, the water-quenched alloy after peak aging also has the highest strength, elongation, and corrosion resistance, which is due to the high driving force and increased number density of aging precipitates, and the narrowed precipitate free zones.
Key words: Al−Zn−Mg−Cu−Zr−Er alloy; quenching rate; aging treatment; precipitate; strengthening

1 Introduction

Al−Zn−Mg−Cu alloys have been used as ideal engineering materials in the aerospace and drilling field due to their high specific strength, low density and high fracture toughness [1−4]. The high strength of the alloys is obtained mainly by solid solution, quenching and aging treatments [5−7]. However, Al−Zn−Mg−Cu alloys are sensitive to the quenching rate, and slow quenching always decreases the strength of the peak-aged alloys [8−10]. The quench sensitivity is mainly caused by the heterogeneous precipitation of equilibrium phase η in the matrix and grain boundaries during the slow quenching process, which reduces the supersaturation of solute atoms and as-quenched vacancies, and thus decreases the strengthening effect in the subsequent aging treatment [11−13]. To obtain a supersaturated solid solution, the alloys are generally quenched into cold water after solution treatment. However, large components or thick plates made of these alloys may not be fully quenched thoroughly in water due to the difference in quenching rates between the surface and middle layer. This results in the residual stress and uneven properties of the alloys, which is not conducive to the application of alloys. Therefore, slow quenching (such as air cooling and oil quenching) is often used in industry to reduce the residual stress in the Al−Zn−Mg−Cu alloys. To satisfy a range of product requirements, it is important to study how the mechanical and corrosion properties change in the alloys quenched

Corresponding author: Xiao-dong WU, Tel: +86-18581029651, E-mail: xiaodongwu@cqu.edu.cn;
Ling-fei CAO, Tel: +86-13996310689, E-mail: caolingfei@cqu.edu.cn
DOI: 10.1016/S1003-6326(22)65856-4
1003-6326/© 2022 The Nonferrous Metals Society of China. Published by Elsevier Ltd & Science Press

in different media [14].

Up to now, there are few reports on the effect of quenching rate on precipitation, especially precipitation at the early aging stage. The atom probe tomography (APT) technique is an effective method to study the early phase decomposition at the atomic scale of age-hardenable aluminum alloys. LIU et al [15] used APT and transmission electron microscopy (TEM) to investigate the effects of quenching rate on strengthening behavior of an Al−Zn−Mg−Cu−Zr alloy during natural aging. It has been discovered that the air-cooled alloy exhibits higher hardness and strength than the rapid water-cooled one during natural aging for up to 30000 h. However, the morphology, density, size, and chemistry of clusters for artificial aged 7xxx aluminum alloy have not yet been reported.

A novel Al−Zn−Mg−Cu alloy with Er and Zr additions was developed in our previous study [16]. The new alloy exhibits good comprehensive properties, such as high strength, recrystallization resistance and corrosion resistance, because of the core-shell $L1_2$-$Al_3(Er_xZr_{1-x})$ particles existing in the alloy [17,18]. These particles can pin the dislocations and (sub)grain boundaries to improve the strength and inhibit the recrystallization [19−21] and they also have high thermal stability even at high temperatures. However, the effects of different quenching media on the age-hardening behavior of the Al−Zn−Mg−Cu−Zr−Er alloy have rarely been reported.

Therefore, to further investigate the quenching and aging characteristics of the new Al−Zn−Mg−Cu−Zr−Er alloy, besides its recrystallization behavior [16], the microstructure and properties of the alloy quenched in three different media were studied in this work. Specifically, the evolution of clusters/precipitates in as-quenched and aged alloys with different quenching rates, which were analyzed by TEM and APT analyses, is the highlight of this work. This work can contribute to the understanding of the relationship between the microstructure and properties of Al−Zn−Mg−Cu−Zr−Er alloys in as-quenched and peak-aged conditions after quenching into different media, and benefit the application of the alloy in industry.

2 Experimental

The material used in this study was Al−6.2Zn−2.0Mg−1.6Cu−0.1Zr−0.1Er, wt.% (Al−2.7Zn−2.3Mg−0.7Cu−0.03Zr−0.02Er, at.%) provided by Southwest Aluminum Co., Ltd., China. The ingots were produced by vertical direct chill (VDC) casting, with a nominal melt temperature of 730 °C and a casting speed of 80 mm/min. The homogenization was designed as a two-stage process ((350 °C, 10 h) + (470 °C, 24 h), with a heating rate of 35 °C/h) followed by air cooling. The alloy was then hot-extruded at 380−430 °C into pipes of *d*150 mm × 12.5 mm (wall thickness) (the extrusion ratio was 10:1). Specimens with a cross-section of 25 mm × 20 mm and 4 mm in thickness were cut from the center of the cross-section of the extrusion parts, parallel to the extrusion direction. The specimens were solution-treated at 470 °C for 2 h, rapidly quenched in different quenching media: water (WQ), oil (OQ), and air (AQ). The cooling curves after solution treatment were measured using embedded thermo-couples, and the temperature−time curves are shown in Fig. 1. The average cooling rates were measured to be about 200 °C/s for water quenching, 50 °C/s for oil cooling, and 2 °C/s for air cooling (by calculating the values in the critical temperature range cooling from 450 to 100 °C). After cooling to room temperature, the samples quenched in different media were immediately aged at 120 °C in an oil bath and quenched in water at intervals to measure the hardness of alloy during aging.

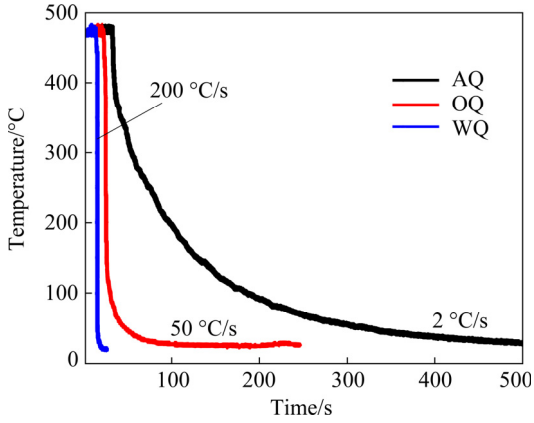

Fig. 1 Cooling curves for quenching into water, oil and air

The Vickers hardness was tested by an MH−5L hardness tester with a load of 9.8 N for 15 s. All the values were averages of 10 measurements across each sample. The tensile test was carried out on an MTS810 material testing system at room

temperature, and the gauge length of the tensile samples was 20 mm at a speed of 1 mm/min. The yield strength ($\sigma_{0.2}$), ultimate tensile strength (σ_b), and elongation (δ) were obtained from the stress−strain curves.

The intergranular corrosion (IGC) test was undertaken in a solution of 1.0 mol/L NaCl + 0.01 mol/L H_2O_2 at (35±3) °C for 6 h according to the standard GB/T 7998—2005 [22]. The corroded surface and maximum corrosion depth were examined using a Zeiss 40 MAT optical microscope (OM).

The morphological characterization and semi-quantitative composition analysis of the phases in the tested alloy were studied by a scanning electron microscope (SEM, Tescan Vega 3) equipped with the energy dispersive X-ray spectroscope (EDS, Oxford INCA).

The precipitates in the grain interior and at grain boundaries of samples under different quenching rates were observed by a transmission electron microscope (TEM, JEOL JEM−2100). The TEM specimens were punched, ground and twin jet electropolished in a solution of HNO_3 and CH_3OH (1:3 in volume) at −30 °C.

Atom probe tomography (APT) analysis was performed using a Cameca Leap 4000HR instrument, which was operated at −248 °C, a voltage pulse fraction of 15%, and a detector efficiency of 36%. The APT data reconstruction and quantitative analysis were performed on the software IVAS 3.8. Moreover, the nearest neighbor distribution (NND) analysis was employed to reveal the distribution of solute atoms in the alloys. The cluster identification parameters with d=0.4 nm (the nearest neighbor distance), and N_{min}=10 (clusters with the minimum solute atoms) were tested carefully to ascertain the distribution and composition of the clusters quenched in different quenching media.

3 Results

3.1 Hardness and tensile properties

The aging curves of the Al−Zn−Mg−Cu−Zr−Er alloy at 120 °C after quenching in different media are shown in Fig. 2. The hardness of the alloy in the as-quenched condition from high to low is as follows: AQ (HV 134) > OQ (HV 122) > WQ (HV 108), which is inversely proportional to the quenching rate. The hardness increment of AQ sample relative to the hardness of WQ sample is HV 26 (accounting for 24%). The hardness increment of the three alloys increases rapidly at the early stage of aging and then slows down to the peak value, followed by a slow decrease. The WQ and OQ samples reach the peak aging hardness at 24 h, and the hardness values are HV 204 and HV 182, respectively. As for the AQ sample, the hardness increases slowly during aging at 120 °C and reaches the peak value of HV 157 at 20 h, which is 23% lower than that of the WQ sample.

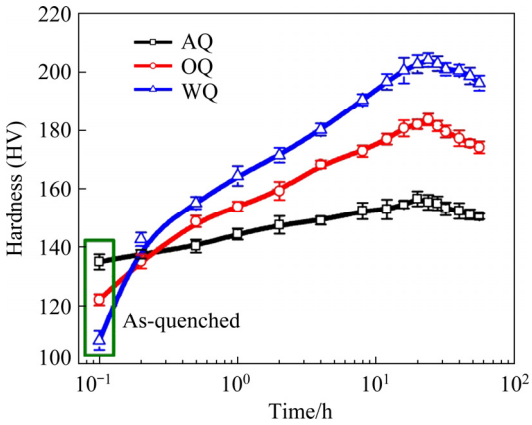

Fig. 2 Aging curves of Al−Zn−Mg−Cu−Zr−Er alloy quenched in different media and aged at 120 °C

Figure 3 shows the engineering stress−engineering strain curves of the peak-aged Al−Zn−Mg−Cu−Zr−Er alloy after quenching in different media. The yield strength ($\sigma_{0.2}$), ultimate tensile strength (σ_b), and elongation (δ) of the tested alloys are shown in Table 1. The lowest strength and elongation are revealed in the AQ sample, whereas the highest ones are exhibited in the WQ sample. The strength loss between a rapid quenching and a slow cooling rate reflects the quenching sensitivity of the alloy [23]. In general, the reduction of $\sigma_{0.2}$ of the alloy is chosen as the index of quenching sensitivity, and a Q-value is introduced here to represent the percentage of $\sigma_{0.2}$ reduction between water- quenched and oil- or air-quenched samples after peak aging, which is defined as [23]

$$Q=\frac{\sigma_{0.2\,\mathrm{WQ}}-\sigma_{0.2}}{\sigma_{0.2\,\mathrm{WQ}}}\times 100\% \quad (1)$$

According to this definition, the quenching sensitivity increases with the higher Q-value. The Q-values of the Al−Zn−Mg−Cu−Zr−Er alloy quenched in oil and air are calculated to be 8.3% and 22.7%, respectively.

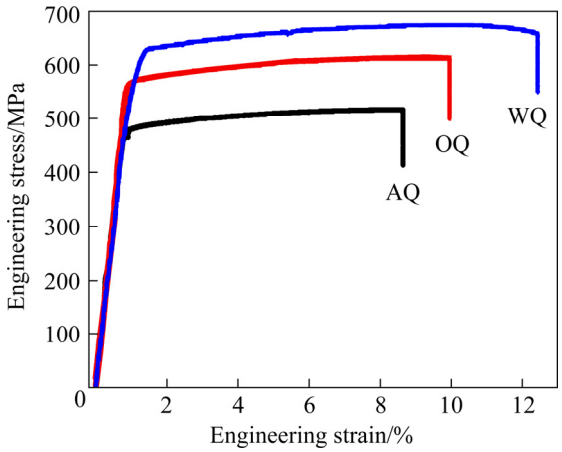

Fig. 3 Engineering stress−strain curves of peak-aged alloy after quenching in different media

Table 1 Tensile properties of peak-aged Al−Zn−Mg−Cu−Zr−Er alloy after quenching in different media

Sample condition	$\sigma_{0.2}$/MPa	σ_b/MPa	δ/%
AQ	482	515	8.6
OQ	572	614	10.0
WQ	624	673	12.5

Figure 4 shows typical fracture surfaces after the tensile testing of the peak-aged alloys. The fracture surface of the AQ sample is dominated by intergranular tear ridges fracture. By contrast, the combination of intergranular fracture and transgranular fracture (dimples) is found in the OQ and WQ samples. The WQ sample shows a higher proportion of transgranular fracture mode, which is consistent with the highest elongation in Table 1.

3.2 Intergranular corrosion of peak-aged alloys

The IGC surfaces and the maximum corrosion depths of the peak-aged alloys are illustrated in Fig. 5. The AQ sample shows the worst surface with large corrosion pits and products (Fig. 5(a)). However, with the increase of quenching rates, the corrosion surfaces of OQ and WQ samples become cleaner and smoother (Figs. 5(b) and (c)), and there are only some small corrosion pits on the WQ sample. The maximum corrosion depth shows the same tendency which increases in the following order: WQ (30.6 μm) < OQ (68.5 μm) < AQ (94.2 μm), as shown in Figs. 5(d−f). Based on the IGC tests, it can be derived that the corrosion resistance of the samples increases in the following order: AQ < OQ < WQ.

3.3 Microstructures of as-quenched alloys

The microstructures of the as-quenched samples were observed by using SEM, TEM, and APT. Considering the sample transfer and preparation time, in fact, each sample for SEM and APT has been natural aged for about 1 h, and TEM sample for 2 h (the samples are kept in liquid nitrogen to inhibit the natural aging process at other time).

The SEM images at low magnification of the typical precipitates near grain boundaries in the as-quenched samples are shown in Fig. 6. In the AQ sample (Fig. 6(a)), the discontinuous η phases (with the size of less than 1 μm) are visible at the grain boundaries of the elongated grains. Besides, dense large η phases also precipitate in the grain interior of the as-quenched AQ sample. Unlike AQ sample, there are many small phases distributed along subgrain boundaries in the as-quenched OQ sample, and some of the precipitates within the grain also become invisible (Fig. 6(b)). As for the as-quenched

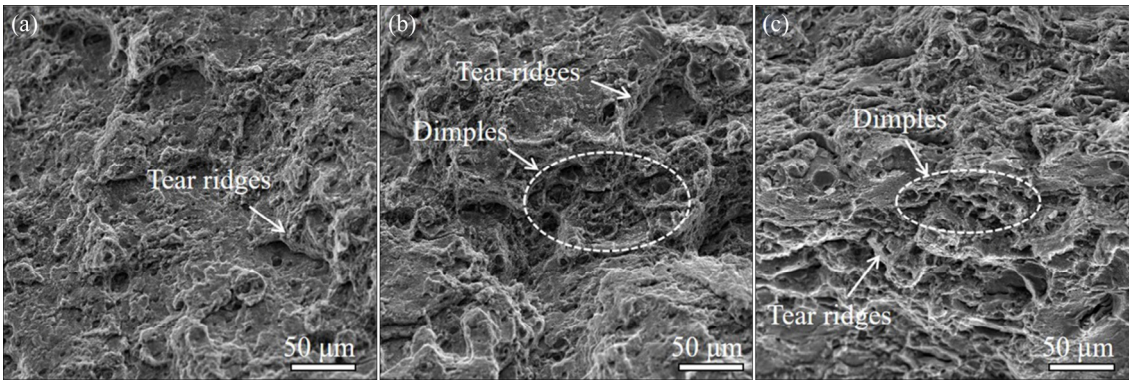

Fig. 4 Tensile fracture morphologies of peak-aged Al−Zn−Mg−Cu− Zr−Er alloys after quenching in different media: (a) AQ; (b) OQ; (c) WQ

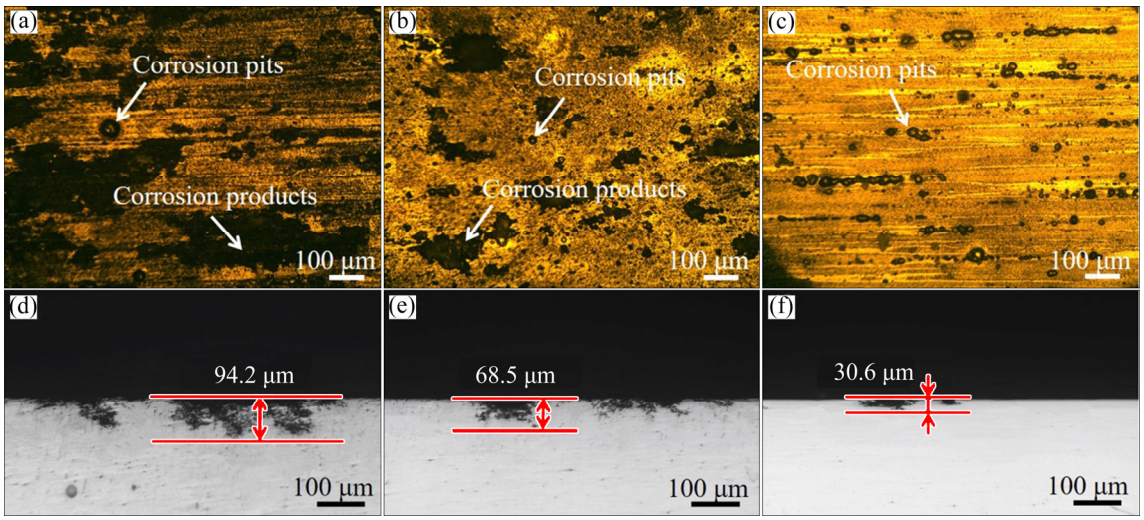

Fig. 5 Surface corrosion morphologies (a−c) and maximum corrosion depths of cross-sections (d−f) for alloys exposed to IGC testing: (a, d) AQ; (b, e) OQ; (c, f) WQ

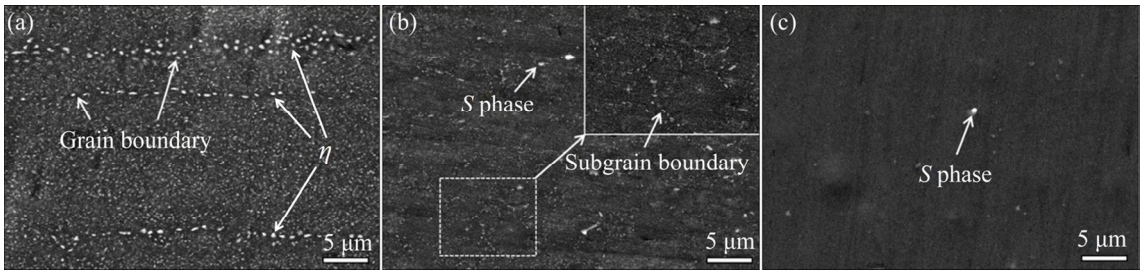

Fig. 6 Backscattered electron SEM images showing large η and S phases in grain interior and at grain boundary of as-quenched alloys: (a) AQ; (b) OQ; (c) WQ

WQ sample with the highest quenching rate, almost no precipitates can be seen in the alloy at SEM scale, and there are only several residual S-Al_2CuMg phases (with size less than 1 μm) can be observed, as shown in Fig. 6(c).

The typical bright field TEM images of the as-quenched alloys are shown in Fig. 7. High-density $Al_3(Er,Zr)$ particles exist in all the alloys with different quenching rates. These particles are precipitated during the homogenization treatment and do not change in the subsequent heat treatments due to their high thermal stability [16]. Therefore, the size and distribution of $Al_3(Er,Zr)$ particles in the three as-quenched alloys are not significantly different. Besides, in the AQ sample, plenty of quench-induced η phases with a length of more than 100 nm are formed in the grains (Fig. 7(a)). The η phases become smaller in the OQ sample (Fig. 7(c)), and there are few large η phases observed in the WQ sample (Fig. 7(e)).

The precipitation sequence in Al−Zn−Mg−Cu alloy with a high Zn/Mg mass ratio (>2.2) is generally as follows: SSS → clusters → GP zones → η' phase → η phase [16,24]. Plenty of clusters are formed at the beginning of aging process, which cannot be detected by TEM. So, APT analyses were used to observe the clusters formed at the early stage of natural aging. Figure 8 shows cluster maps of the as-quenched alloys that inevitably undergo natural aging for 1 h, and for good visualization, the selected analysis boxes are shown in the same size (100 mm × 30 mm × 30 nm) and the Al, Zn, Mg and Cu atoms are present in the clusters (for better visualization, the atom sizes in the maps have been adjusted). The clusters with 10−50 atoms are observed in all three as-quenched alloys after quenching in different media. The number density (N_V) of clusters gradually decreases with the increase of quenching rate, and the N_V of clusters in AQ, OQ and WQ samples is 43.9×10^{23}, 12.8×10^{23} and 4.3×10^{23}/m^3, respectively. It can be seen from the partially enlarged view on the right of

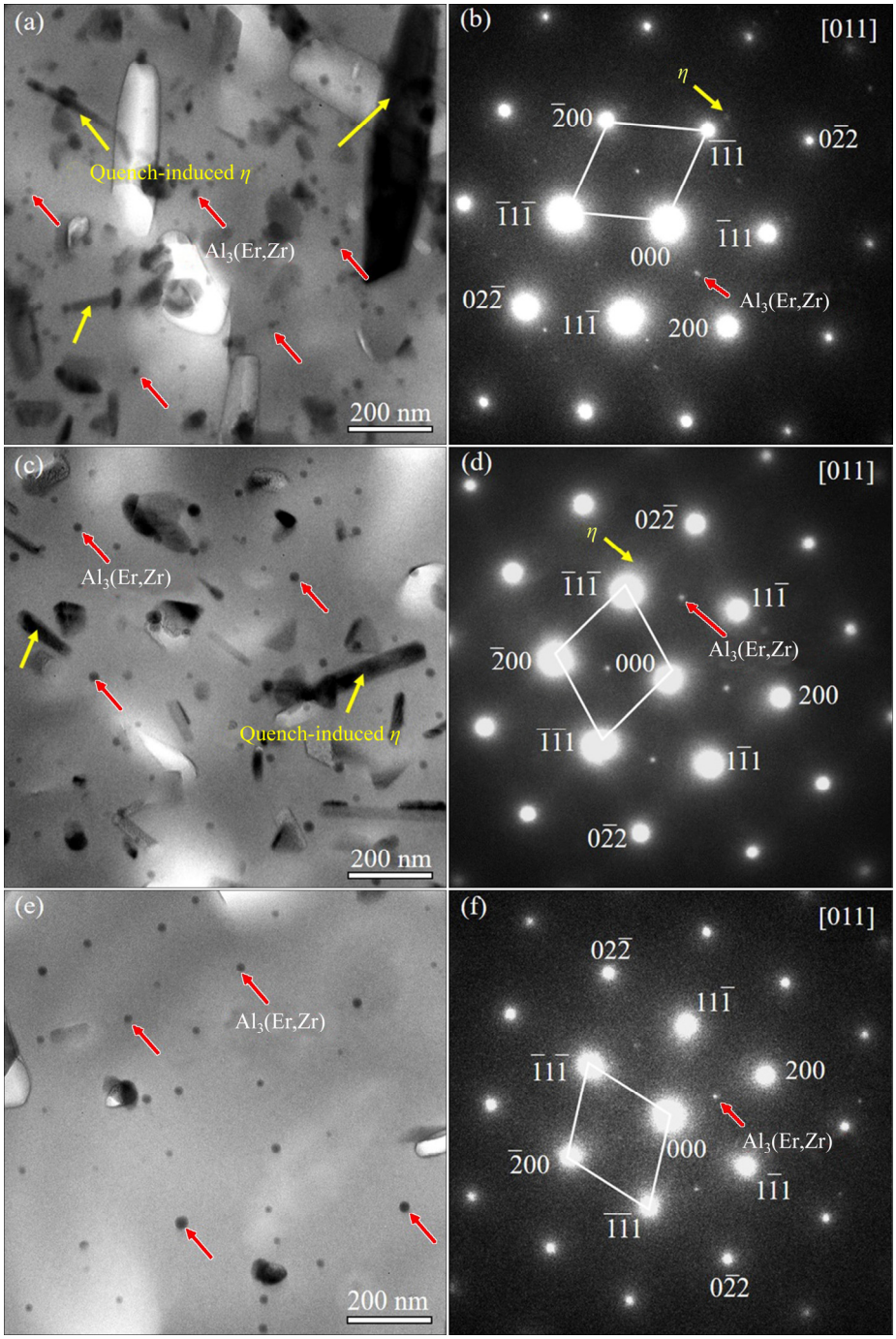

Fig. 7 Typical bright field TEM images and corresponding SAED patterns of as-quenched alloys: (a, b) AQ; (c, d) OQ; (e, f) WQ (Images are taken along the $\langle 011 \rangle_{Al}$ zone axis)

each analysis box that the clusters in the as-quenched alloys have irregular shapes and no big difference in size. The average spacing of clusters increases with the increase of the quenching rate.

From the APT cluster maps, it can be seen that the solute clusters are enriched with Zn, Mg and Cu atoms. As shown in Fig. 9, the NNDs (to reveal the distribution of solute atoms in the alloys) of Zn, Mg and Cu atoms in the experimental data sets (black lines) deviate slightly from the reference NNDs of corresponding random data sets (red lines) in all three alloys. Besides, for the same element, the deviation of the solute atoms becomes smaller with the increase of quenching rate (Figs. 9(a) to (c)), and this phenomenon is especially obvious for Cu atoms. This suggests that the distribution of the solute atoms becomes more non-random in the matrix for the as-quenched AQ sample, in other

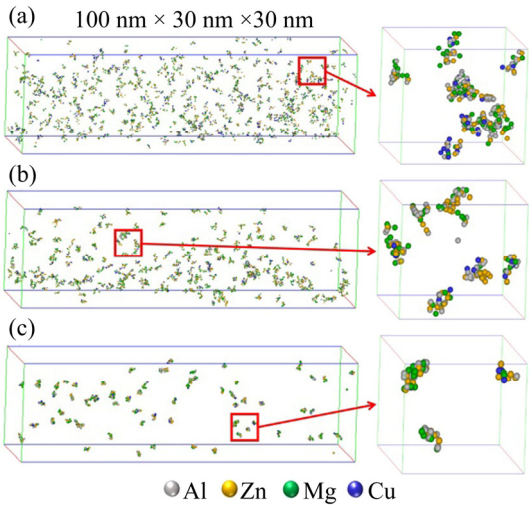

Fig. 8 Cluster maps (100 mm × 30 mm × 30 nm) of as-quenched alloys (N_{min}=10, d=0.6 nm): (a) AQ; (b) OQ; (c) WQ (The atom sizes in the maps have been adjusted for better visualization)

words, more distinct clusters are formed in the AQ sample. This is also consistent with the cluster distribution in Fig. 8.

Figure 10 shows the histograms and Gaussian fitting curves of the frequency of clusters with different atom numbers in the three as-quenched alloys. Clusters in the as-quenched condition mostly consist of 15−25 atoms. The average atom number of the clusters increases with the decrease of the quenching rate, and there are almost no clusters with more than 50 atoms in the as-quenched alloys except the AQ sample.

The solute composition of the clusters in the alloy quenched in various media is also different. To clarify the change of solute in clusters, their average contents in the as-quenched condition are shown in Fig. 11. The contents of solute atoms (Zn, Mg and Cu) of the clusters decrease gradually in the AQ, OQ and WQ samples, while the content of Al atoms increases from 36.1 at.% to 40.9 at.%. Besides, compared with WQ sample, the Cu content in AQ sample increases by about 17%, which is higher than the increments of Zn (9%) and Mg (5%). This is consistent with the higher content of Cu atoms (in blue) in the clusters of AQ sample in the enlarged view of Fig. 8(a).

3.4 Microstructure of peak-aged alloys

After peak-aging treatment, the mechanical properties of the three alloys reach the highest level.

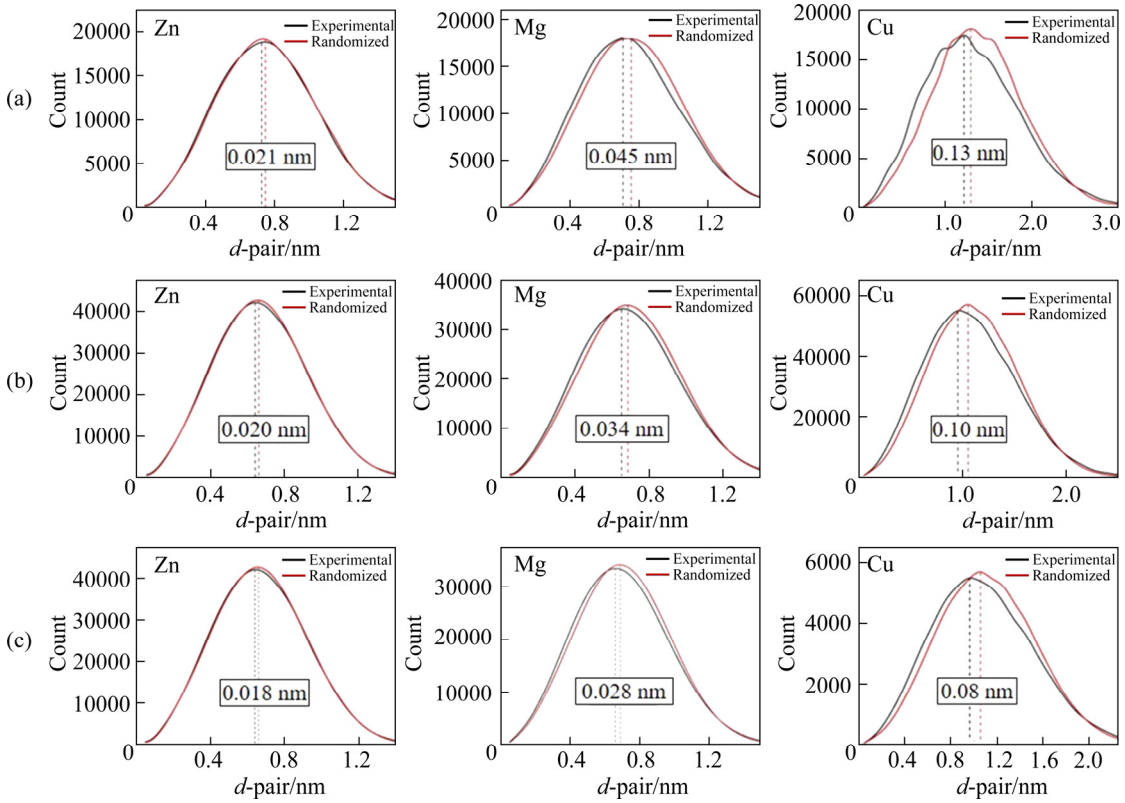

Fig. 9 NND analysis of solute atoms in as-quenched alloys: (a) AQ; (b) OQ; (c) WQ (d-pair is the distance between pairs of solute atoms)

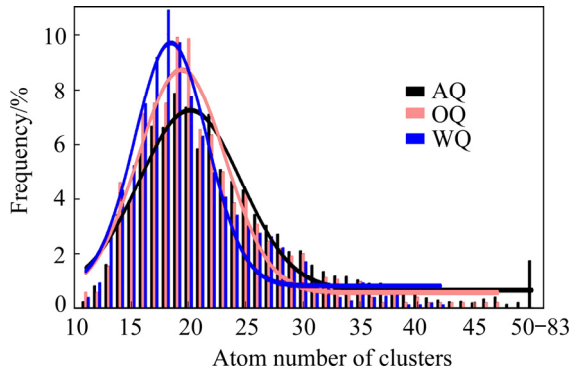

Fig. 10 Frequency of clusters with different atom numbers in as-quenched alloys (The experimental data are fitted by the normal distribution (Gaussian) curves (solid lines))

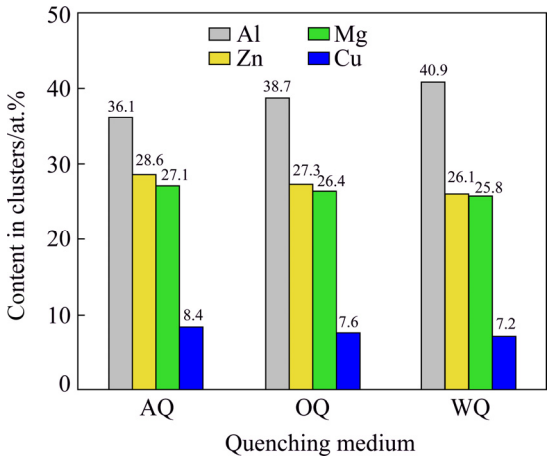

Fig. 11 Average contents of clusters in as-quenched alloys

Figure 12 shows typical TEM images at higher magnification of the η' precipitates within the grains and η phases along grain boundaries of the peak-aged alloys. The plate-like η' precipitates with an average diameter of about 10 nm are formed in the peak-aged AQ sample (Fig. 12(a)). The size of η' precipitates (diameter of about 5 nm) in the WQ sample decreases, and the number density increases significantly, as shown in Fig. 12(c), while those of the OQ sample are between WQ and AQ samples (Fig. 12(b)). Besides, a wide precipitate free zone (PFZ) with a width of 102.6 μm is observed in the AQ sample (Fig. 12(d)), whereas narrower PFZs are found in OQ and WQ samples with widths of 70.3 and 52.3 nm, respectively (Figs. 12(e, f)).

To obtain the change of the precipitates during aging, APT analysis was also performed on the peak-aged WQ sample. As shown in Fig. 13, plenty

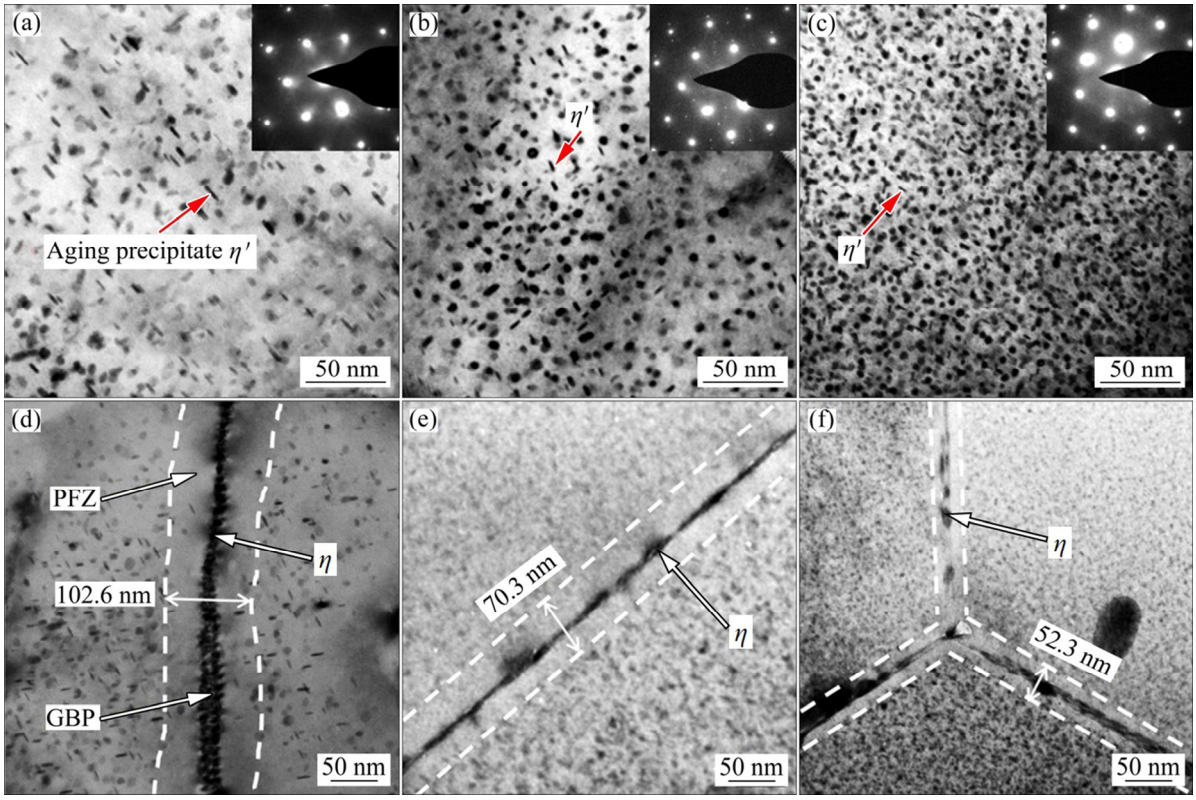

Fig. 12 TEM micrographs of peak-aged alloys: (a, d) AQ; (b, e) OQ; (c, f) WQ (Images are taken along $\langle 011 \rangle_{Al}$ zone axis)

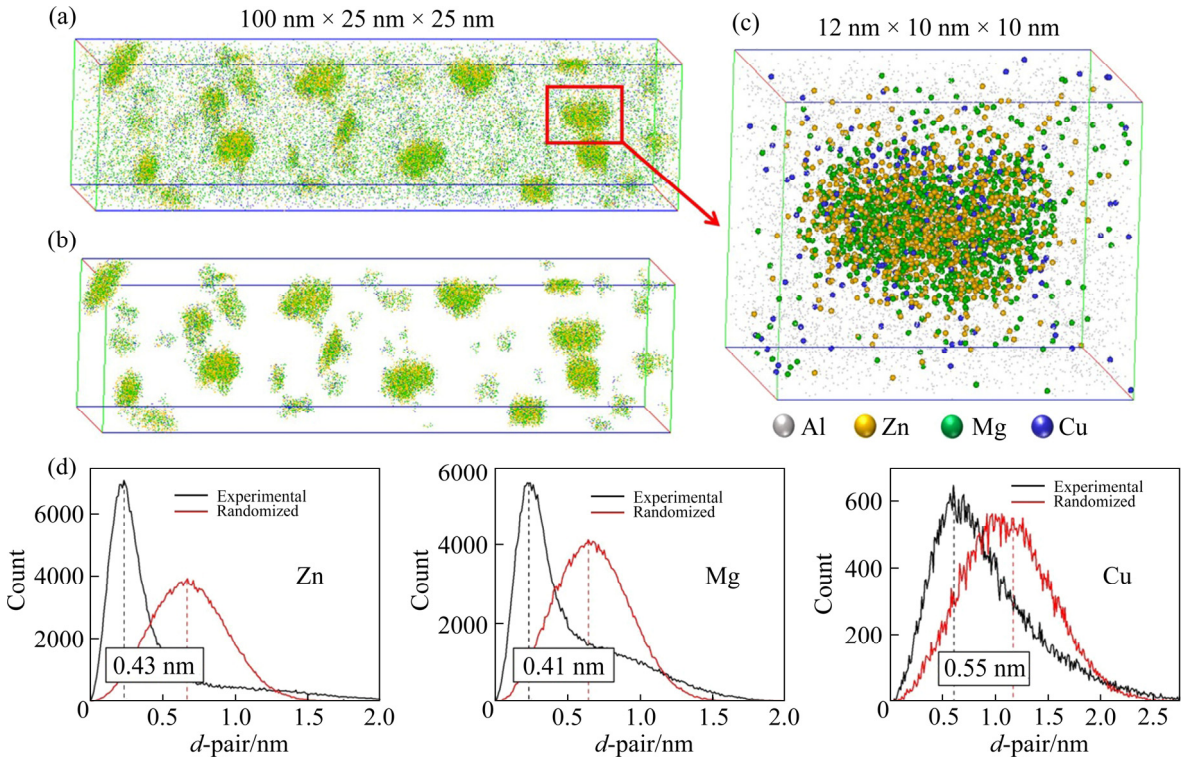

Fig. 13 APT atom maps (100 nm × 25 nm × 25 nm) (a), cluster maps (b) and APT elemental mapping of η' (c) of peak-aged WQ alloy, and NND analysis of solute atoms in peak-aged WQ alloy (d) (N_{min}=10, d=0.6 nm, and the atom sizes in the maps have been adjusted for better visualization)

of η' precipitates with diameters of 6−12 nm can be observed. The partially enlarged view (Fig. 13(c)) shows that the precipitate in the peak-aged alloy is plate-shaped and contains more solute atoms (usually more than 150 atoms). The contents of Zn, Mg and Cu of the precipitates in the peak-aged WQ alloy increase to 32.3 at.%, 33.2 at.%, and 7.8 at.%, respectively. Besides, from the NND analysis in Fig. 13(d), the deviation of Zn, Mg and Cu atoms in the peak-aged WQ sample becomes larger, indicating that the solute elements in the alloy have obvious segregation and a large number of η' precipitates are formed after aging.

4 Discussion

The compound addition of Zr and Er can form fine dispersed Al_3(Er,Zr) particles with diameters of 15−25 nm in the alloys during homogenization treatment. These particles do not change significantly during the subsequent solution treatment and quenching due to their high thermal stability [14]. The Al_3(Er,Zr) particles introduce an additional strength to improve the mechanical properties of the alloy [16]. Besides, the recrystallization inhibition of Al_3(Er,Zr) particles can further improve the corrosion resistance of the alloy [18]. So, adding Zr and Er can improve the strength and corrosion resistance of the Al−Zn−Mg−Cu alloys, which has been discussed in our previous work [16]. Therefore, in this work, main attention is paid to the influence of quenching rate on microstructure, strengthening behavior and corrosion property of Al−Zn−Mg−Cu−Zr−Er alloy during aging treatment.

The quenching medium has a significant effect on microstructures, which influences the hardness, strength and corrosion resistance of the as-quenched and aged Al−Zn−Mg−Cu−Zr−Er alloys. The as-quenched sample with the slowest quenching rate (AQ, 2 °C/s) has higher hardness than the other samples with higher quenching rates, which is caused by the quench-induced clusters and η phases, as shown in Figs. 7 and 8. The slower quenching rate makes the alloy stay at a higher temperature for a longer time, giving enough time for solute atoms (especially Cu atoms with lower diffusion rate) to diffuse, which leads to possible

decomposition of the supersaturated solid solution to form the equilibrium phase and a large number of clusters [25,26]. On the contrary, when the quenching rate becomes higher, the solute atoms in the alloy have no time to precipitate and finally form a supersaturated solid solution with a higher concentration. This also explains why the average solute content of clusters in Fig. 11 increases with the decrease of quenching rate.

The high mechanical properties of Al−Zn−Mg−Cu alloys are mainly due to the nanoscale strengthening precipitates formed after aging treatment. It is reported that the strength of the peak-aged alloy is dominated by the contributions of the grain boundaries (σ_{gb}), intermetallic particles (σ_p), solute in the matrix (σ_{ss}), clusters ($\sigma_{cluster}$), and precipitates (σ_{ppt}). Thus, the sample strength can be approximated as [24]

$$\sigma_{0.2}=\sigma_0+\sigma_{gb}+\sigma_p+\sigma_{ss}+\sigma_{cluster}+\sigma_{ppt} \quad (2)$$

where σ_0 is the resistance to dislocation glide within the grains for the high-purity aluminum (about 10 MPa for pure Al). The σ_{gb}, σ_p and $\sigma_{cluster}$ tend to be very small (usually only several to a dozen MPa), the σ_{ss} is determined by the content of solute elements in the alloy, and there is no significant difference between the three peak-aged alloys. Therefore, the precipitates make a dominant contribution (σ_{ppt}) to strengthening in the peak-aged alloys [27].

The formation of strengthening precipitates during aging is a process of uniform nucleation, which requires high supersaturated solutes and vacancies. During the slow quenching process, a large number of solute atoms and vacancies are consumed to form quench-induced phases and PFZs. During the subsequent aging treatment, the supersaturation degree of supersaturated solid solution and the nucleation driving force of precipitates decrease. Therefore, the depletion of solute atoms reduces the number density of strengthening precipitates, resulting in a permanent reduction in the strength of the slow-quenched alloy. Besides, the low density of vacancies is not conducive to the uniform dispersion of strengthened precipitates. When the AQ sample is aged at 120 °C, the quenched-induced clusters grow and coalesce into precipitates with larger size and low number density. As a result, the hardness of AQ alloy rises slowly during aging and the peak-aged strength is pretty low. With the increasing quenching rate, the subsequent age-hardening rate and peak-aged strength of the OQ (50 °C/s) and WQ (200 °C/s) samples increase. The highest hardness increment of the peak-aged WQ sample is likely attributed to the highest number density of η' as shown in Figs. 12(a−c).

The decrease of the quenching rate also increases the width of PFZs near grain boundaries, as shown in Figs. 12(d−f). The grain boundary is a kind of planar defect, which is often a favorable location for equilibrium nucleation and a fast diffusion channel for solute atoms [28]. The PFZs are formed adjacent to grain boundaries, dislocations, or precipitates and they are caused by either solute or vacancy depletion. It is reported that the PFZs formed by vacancy depletion tend to shrink while those controlled by solute depletion tend to expand with aging time [29]. Besides, vacancy depletion tends to dominate at the early stage of aging, while solute depletion dominates after a long aging period [30]. The relationship between vacancy and solute depleted PFZs during aging has been studied by CHANG and MORRAL [29]. During the air-cooling process, a large number of equilibrium phases nucleate and grow at grain boundaries, while in the subsequent aging treatment, the phases further grow and coarsen by absorbing the solutes around, leading to the depletion of the surrounding solutes. In addition, the as-quenched vacancies diffuse to the grain boundary during the slow cooling, resulting in the decrease of vacancy concentration near the grain boundary. Therefore, there are no strengthening precipitates formed in these areas during aging, and eventually, the wide PFZs are formed along grain boundaries in the slowly-quenched alloy, as shown in Fig. 12(d).

The plasticity of the peak-aged alloys after quenching in various media is different, which is mainly related to the width of PFZs near grain boundaries. The η precipitates are formed along the grain boundary and grow by absorbing the surrounding solutes. Finally, the solute concentration decreases and the PFZs are formed near the grain boundary [31]. The wide PFZ in the AQ sample has lower strength, so the intergranular fracture is easy to crack along the PFZs during deformation [32]. On the contrary, the peak-aged WQ sample exhibits the highest plasticity with

transgranular fracture because the narrower PFZ contributes to the uniform deformation of the alloy [16]. Besides, the finer η' precipitates are uniformly distributed in the matrix of WQ sample. Dislocations in the alloy pass through the fine η' precipitates (semi-coherent with the α(Al) matrix) mainly through cutting or bypassing mechanisms. The uniform distribution of fine η' precipitates can make the dislocations evenly stressed, reducing dislocation accumulation and stress concentration. Hence, the deformation of the WQ alloy is more homogeneous and the plasticity is improved. To sum up, the higher quenching rate increases both the strength and plasticity of the Al−Zn−Mg−Cu−Zr−Er alloy.

The PFZs and grain boundary precipitates (GBP) η can also affect the corrosion resistance of the aluminum alloys. The anodic η phases at grain boundaries tend to be aggregated preferentially and provide preferential channels for crack propagation. Furthermore, the wide PFZs near grain boundaries have also been proved to decrease the corrosion resistance of the alloy [33]. Due to the difference in potential between PFZs and anodic η phases along grain boundaries, the localized corrosion starts at the interface between them, which leads to severe intergranular corrosion cracks in the AQ sample. Therefore, the Al−Zn−Mg−Cu−Zr−Er alloy with a faster quenching rate has better mechanical properties, plasticity and corrosion resistance.

5 Conclusions

(1) The as-quenched Al−Zn−Mg−Cu−Zr−Er alloy with the slowest quenching rate (air-cooling) has a higher hardness than the water-quenched one, which is attributed to the presence of quench-induced η phase and a large number of clusters in the alloy.

(2) With the decreasing quenching rate, the age-hardening rate decreases significantly during the aging treatment. Due to the strong nucleation driving force of precipitates in the water-quenched alloy, plenty of strengthening precipitates η' are formed during aging, thus the peak-aged alloy shows the highest mechanical properties.

(3) The solute depletion during the slow quenching leads to the widest PFZs of the air-cooled sample, which reduces the elongation and corrosion resistance of the alloy.

Acknowledgments

The authors are grateful for the financial supports from the National Natural Science Foundation of China (No. 51871033), and the Opening Project of State Key Laboratory for Advanced Metals and Materials, China (No. 2020-ZD02).

References

[1] HUTCHINSON C R, de GEUSER F, CHEN Y, DESCHAMPS A. Quantitative measurements of dynamic precipitation during fatigue of an Al−Zn−Mg−(Cu) alloy using small- angle X-ray scattering [J]. Acta Materialia, 2014, 74: 96−109.

[2] ZHU Qian-qian, CAO Ling-fei, LIU Ya-hui, LIU Shi-feng, WU Xiao-dong. Intergranular micro-deformation behavior of a medium strength 7xxx aluminum alloy [J]. Journal of Materials Research and Technology, 2021, 12: 471−477.

[3] PENG Xiao-yan, GUO Qi, LIANG Xiao-peng, DENG Ying, GU Yi, XU Guo-fu, YIN Zhi-min. Mechanical properties, corrosion behavior and microstructures of a non-isothermal ageing treated Al−Zn−Mg−Cu alloy [J]. Materials Science and Engineering A, 2017, 688: 146−154.

[4] CHEN Jun-zhou, ZHEN Liang, YANG Shou-jie, SHAO Wen-zhu, DAI Sheng-long. Investigation of precipitation behavior and related hardening in AA 7055 aluminum alloy [J]. Materials Science and Engineering A, 2009, 500(1/2): 34−42.

[5] YANG B, MILKEREIT B, ZHANG Y, ROMETSCH P A, KESSLER O, SCHICK C. Continuous cooling precipitation diagram of aluminium alloy AA7150 based on a new fast scanning calorimetry and interrupted quenching method [J]. Materials Characterization, 2016, 120: 30−37.

[6] PENG Ying-hao, LIU Chong-yu, WEI Li-li, JIANG Hong-jie, GE Zhen-jiang. Quench sensitivity and microstructures of high-Zn-content Al−Zn−Mg−Cu alloys with different Cu contents and Sc addition [J]. Transactions of Nonferrous Metals Society of China, 2021, 31: 24−35.

[7] LV Qing, LIU Zhi-yi, DUAN Shui-liang, LI Yao. Effect of quenching medium and small addition of Ag on microstructure and properties of Al−Zn−Mg−Cu alloy [J]. Transactions of Materials and Heat Treatment, 2009, 30: 92−95.

[8] WANG Yi-chang, CAO Ling-fei, WU Xiao-dong, ZOU Yan, HUANG Guang-jie. Research progress on microstructure and properties of 7xxx series aluminum alloys for oil drill pipes [J]. Materials Reports, 2019, 33: 1190−1197.

[9] ZHENG Yu-lin, LI Cheng-bo, LIU Sheng-dan, DENG Yun-lai, ZHANG Xin-ming. Effect of homogenization time on quench sensitivity of 7085 aluminum alloy [J]. Transactions of Nonferrous Metals Society of China, 2014, 24: 2275−2281.

[10] LIU Sheng-dan, LIAO Wen-bo, TANG Jian-guo, ZHANG Xin-ming, LIU Xin-yu. Influence of exfoliation corrosion on tensile properties of a high strength Al−Zn−Mg−Cu alloy [J]. Journal of Central South University, 2013, 20(1): 1−6.

[11] LIU Sheng-dan, ZHONG Qi-min, ZHANG Yong, LIU Wen-Jun, ZHANG Xin-ming, DENG Yun-lai. Investigation of quench sensitivity of high strength Al−Zn−Mg−Cu alloys by time−temperature−properties diagrams [J]. Materials & Design, 2010, 31(6): 3116−3120.

[12] KANG Lei, ZHAO Gang, WANG Guang-dong, LIU Kun, TIAN Ni. Effect of different quenching processes following solid-solution treatment on properties and precipitation behaviors of 7050 alloy [J]. Transactions of Nonferrous Metals Society of China, 2018, 28: 2162−2172.

[13] LIU Sheng-dan, LIU Wen-Jun, ZHANG Yong, ZHANG Xin-ming, DENG Yun-lai. Effect of microstructure on the quench sensitivity of AlZnMgCu alloys [J]. Journal of Alloys and Compounds, 2010, 507: 53−61.

[14] WU Hao, WEN Sheng-ping, HUANG Hui, GAO Kun-yuan, WU Xiao-lan, WANG Wei, NIE Zuo-ren. Hot deformation behavior and processing map of a new type Al−Zn−Mg−Er−Zr alloy [J]. Journal of Alloys and Compounds, 2016, 685: 869−880.

[15] LIU Sheng-dan, ZHANG Meng-han, LI Qun, ZHU Qian-qian, SONG Hui, WU Xiao-dong, CAO Ling-fei, COUPER J M. Effect of quenching rate on strengthening behavior of an Al−Zn−Mg−Cu alloy during natural ageing [J]. Materials Science and Engineering A, 2020, 793: 139900.

[16] WANG Yi-chang, WU Xiao-dong, CAO Ling-fei, TONG Xin, COUPER J M, LIU Qing. Effect of trace Er on the microstructure and properties of Al−Zn−Mg−Cu−Zr alloys during heat treatments [J]. Materials Science and Engineering A, 2020, 792: 139807.

[17] WU Hao, WEN Sheng-ping, LU Jun-tai, MI Zhen-peng, ZENG Xian-long, HUANG Hui, NIE Zuo-ren. Microstructural evolution of new type Al−Zn−Mg−Cu alloy with Er and Zr additions during homogenization [J]. Transactions of Nonferrous Metals Society of China, 2017, 27: 1476−1482.

[18] NIE Zuo-ren, WEN Sheng-ping, HUANG Hui, LI Bo-long, ZUO Tie-yong. Research progress of Er-containing aluminum alloy [J]. The Chinese Journal of Nonferrous Metals, 2011, 21: 2361−2370. (in Chinese)

[19] WEN Sheng-ping, GAO Kun-yuan, HUANG Hui, WANG Wei, NIE Zuo-ren. Precipitation evolution in Al−Er−Zr alloys during aging at elevated temperature [J]. Journal of Alloys and Compounds, 2013, 574: 92−97.

[20] CHEN Jing, PAN Qing-lin, YU Xue-hong, LI Meng-jia, ZOU Hao, XIANG Hao, HUANG Zhi-qi, HU Quan. Effect of annealing treatment on microstructure and fatigue crack growth behavior of Al−Zn−Mg−Sc−Zr alloy [J]. Journal of Central South University, 2018, 25(5): 961−975.

[21] XIAO Quan-feng, HUANG Ji-wu, JIANG Ying-ge, JIANG Fu-qin, WU Yun-feng, XU Guo-fu. Effects of minor Sc and Zr additions on mechanical properties and microstructure evolution of Al−Zn−Mg−Cu alloys [J]. Transactions of Nonferrous Metals Society of China, 2020, 30: 1429−1438.

[22] GB 7998—2005. Test method for intergranular corrosion of aluminium alloy [S].

[23] LIN Liang-hua, LIU Zhi-yi, BAI Song, ZHOU Ya-ru, LIU Wen-juan, LV Qing. Effects of Ge and Ag additions on quench sensitivity and mechanical properties of an Al−Zn−Mg−Cu alloy [J]. Materials Science and Engineering A, 2017, 682: 640−647.

[24] WANG Yi-chang, WU Xiao-dong, CAO Ling-fei, TONG Xin, ZOU Yan, ZHU Qian-qian, TANG Song-bai, SONG Hui, GUO Ming-xing. Effect of Ag on aging precipitation behavior and mechanical properties of aluminum alloy 7075 [J]. Materials Science and Engineering A, 2021, 804: 140515.

[25] TANG Jian-guo, CHEN Hui, ZHANG Xin-ming, LIU Sheng-dan, LIU Wen-jun, OUYANG Hui, LI Hong-ping. Influence of quench-induced precipitation on aging behavior of Al−Zn−Mg−Cu alloy [J]. Transactions of Nonferrous Metals Society of China, 2012, 22: 1255−1263.

[26] KHALFALLAH A, RAHO A A, AMZERT S, DJEMLI A. Precipitation kinetics of GP zones, metastable η' phase and equilibrium η phase in Al−5.46wt.%Zn−1.67wt.%Mg alloy [J]. Transactions of Nonferrous Metals Society of China, 2019, 29: 233−241.

[27] ZOU Yan, CAO Ling-fei, WU Xiao-dong, WANG Yi-chang, SUN Xuan, SONG Hui, COUPER J M. Effect of ageing temperature on microstructure, mechanical property and corrosion behavior of aluminum alloy 7085 [J]. Journal of Alloys and Compounds, 2020, 823: 153792.

[28] UNWIN P N T, LORIMER G W, NICHOLSON R B. The origin of the grain boundary precipitate free zone [J]. Acta Metallurgica, 1969, 17(11): 1363−1377.

[29] CHANG S, MORRAL J E. The influence of quenching rate on precipitate-free-zones in an Al−Zn−Mg alloy [J]. Acta Metallurgica, 1975, 23(6): 685−689.

[30] WANG Tao, YIN Zhi-min. Research status and development trend of ultra-high strength aluminum alloys [J]. Chinese Journal of Rare Metals, 2006, 30: 197−202. (in Chinese)

[31] WANG Yi-chang, CAO Ling-fei, WU Xiao-dong, TONG Xin, LIAO Bin, HUANG Guang-jie, WANG Zheng-an. Effect of retrogression treatments on microstructure, hardness and corrosion behaviors of aluminum alloy 7085 [J]. Journal of Alloys and Compounds, 2020, 814: 152264.

[32] OGURA T, OTANI T, HIROSE A, SATO T. Improvement of strength and ductility of an Al−Zn−Mg alloy by controlling grain size and precipitate microstructure with Mn and Ag addition [J]. Materials Science and Engineering A, 2013, 580: 288−293.

[33] WANG Yu, DENG Yun-lai, CHEN Ji-qiang, DAI Qing-song, GUO Xiao-bin. Effects of grain structure related precipitation on corrosion behavior and corrosion fatigue property of Al−Mg−Si alloy [J]. Journal of Materials Research and Technology, 2020, 9(3): 5391−5402.

不同淬火速率下 Al−Zn−Mg−Cu−Zr−Er 合金的时效析出行为及性能

王一唱[1]，吴晓东[1]，岳 露[1]，郭明星[2]，曹玲飞[1,3]

1. 重庆大学 材料科学与工程学院 轻合金国际联合实验室(教育部)，重庆 400044；
2. 北京科技大学 新金属材料国家重点实验室，北京 100083；
3. 重庆大学 沈阳材料科学国家研究中心，重庆 400044

摘 要：研究淬火速率对 Al−Zn−Mg−Cu−Zr−Er 合金时效析出行为和性能的影响。采用扫描电镜、透射电镜和原子探针层析技术等研究合金中团簇和析出相的析出行为与特征。固溶后冷却速率最慢的空冷合金中会形成淬火诱导 η 相及大量团簇，使其淬火态硬度比水淬合金的提高了 24% (HV 26)。然而，合金的时效硬化响应速度和峰时效硬度随淬火速率的增加而增大，峰时效态的水淬合金具有最高的强度、伸长率和耐蚀性，这是由于水淬合金时效析出驱动力较大，使析出相的数量密度增大及晶间无析出带的宽度减小。

关键词：Al−Zn−Mg−Cu−Zr−Er 合金；淬火速率；时效处理；析出相；强化

(Edited by Wei-ping CHEN)